nature portfolio

https://doi.org/10.1038/s41561-022-01025-x

Supplementary information

Climatic and tectonic drivers of late Oligocene Antarctic ice volume

In the format provided by the authors and unedited

Supplementary Information

S1. GDGT temperature calibrations and non-thermal influences

Isoprenoid GDGTs produced by marine archaea demonstrate an increase in the number of cyclopentane moieties produced as water temperature increases[1,2]. Typically, this relationship has been quantified using the TEX_{86} ratio, which uses a subset of the six commonly analysed GDGTs[1]. However, in the polar ocean where temperatures are below 5°C, variance in TEX_{86} values are relatively minor and have a non-linear relationship with temperature[1,3], and TEX_{86}-based reconstructions do not always reconcile with other well-constrained paleotemperature indicators[4]. TEX_{86}, and other ratios such as the TEX_{86}^{L} ratio, do not necessarily detect non-analogue GDGT distributions in ancient samples as they apply a single parameter to what is a six-dimensional data space[5]. Although various screening methods have been developed to remove non-analogue samples from a TEX_{86} dataset (i.e. the methane index, branched versus isoprenoid index and others as detailed below), these do not provide a fundamental measure of how similar a paleo-GDGT distribution is to those in the modern calibration dataset[5]. To improve temperature estimates, identify non-analogue distributions and better represent uncertainty in paleo samples, Dunkley Jones et al. (2020)[5] developed a machine-learning based approach, the OPTiMAL calibration. This is a multi-dimensional Gaussian Process Regression tool which uses all six GDGTs to provide both SST and uncertainty estimates related to the strength of the relationship between the GDGT distribution of an individual sample and the modern calibration dataset. Non-analogue distributions are identified using a weighted distance metric '$D_{nearest}$'. This nearest neighbour test is a measure of the distance between a sample's GDGT distribution and the most similar sample within the modern calibration dataset. Dunkley Jones et al. (2020)[5] found that samples with $D_{nearest} > 0.5$ are unlikely to be well constrained by any current calibration model. In our Ross Sea sample set, 8 samples have $D_{nearest}$ values above 0.5 and have been removed from our OPTiMAL temperature record (Fig. S1, Fig. S2). Supplementary Table 1 details average SST estimates for the Ross Sea and Wilkes Land[6,7] for timeslices through the Cenozoic, and compares these to other paleoenvironmental information from the Antarctic, demonstrating that OPTiMAL reconstructs temperatures in line with other paleoenvironmental indicators.

Several TEX_{86}-based approaches have also been developed in an effort to better represent high latitude Southern Ocean and Antarctic temperatures, and results using these methods are also presented here (Fig. S2); 1) Kim et al. (2010)[8] found that the regio-isomer of crenarchaeol is strongly correlated with SST at high temperatures, but not at low temperatures. They developed a calibration excluding the crenarchaeol regio-isomer for when expected temperatures are below 15°C (TEX_{86}^{L}). Kim et al. (2012)[8] recognised that Thaumarchaeota have elevated abundances in the subsurface offshore Wilkes Land, Antarctica, and proposed an adjustment to the TEX_{86}^{L} calibration to calibrate it to depth integrated mean annual temperatures from 0-200 m water depth. 2) Shevenell et al. (2011)[9] analysed core top samples from the Antarctic Peninsula and integrated these data into the global core top calibration of Kim et al. (2008) to derive a Holocene record of temperature change. 3) Tierney and Tingley (2014, 2015) developed BAYSPAR[10,11], a Bayesian, spatially varying regression calibration which accounts for the spatial variance in the response of TEX_{86} to temperature in the core top dataset. The use of TEX_{86} and TEX_{86}^{L} based calibrations are subject to screening methods outlined below to remove non-analogue samples from the data set. Figure S3 compares OPTiMAL to these TEX_{86} and TEX_{86}^{L} based methods for the late Oligocene/early Miocene period. TEX_{86}-based approaches (BAYSPAR[10,11] and Shevenell et al., 2011[9]) also demonstrate a gradual cooling trend through this interval. While BAYSPAR Standard reconstructs similar temperatures to OPTiMAL and other Antarctic-proximal paleoenvironmental indicators described in Table S1, BAYSPAR Analogue and the calibration of Shevenell et al. (2011)[9] suggest temperatures that are higher than is supported by paleoenvironmental information. The TEX^{L}_{86} based method[12] shows a more variable trend but includes reconstructed values that are unrealistically cold (i.e. several values below -5 °C). The lack of a late Oligocene warming trend in the TEX_{86}-based methods, coupled with the paleoenvironmental information outlined in Table S1 and the main manuscript demonstrate that our interpretations for the late Oligocene time interval are not a function of our choice of the OPTiMAL calibration.

TEX_{86} and TEX^{L}_{86}-based temperatures can be biased by non-thermal effects and the input of GDGTs from sources other than marine Thaumarchaeota, summarised in the following section.

1) Debate has centred on whether TEX_{86} reflects a sea surface or subsurface temperature. The seasonality of isoGDGT production and export has also been considered a potential bias for TEX_{86}, and suggests that the TEX_{86} values derived from seafloor sediment may be weighted towards a certain season rather than reflecting mean annual temperature[2,13]. In Antarctica, archaea are most abundant in winter and early spring, with maximum abundances in the subsurface at ~100m[14–17]. While OPTiMAL[5] and the calibration of Shevenell et al. (2011)[9] are surface calibrations, Kim et al. (2012) and BAYSPAR can be calibrated to the subsurface[11,12].

2) The BIT (branched versus isoprenoid tetraethers) index is used to assess the contribution of GDGTs from terrestrial soils, based on the abundance of brGDGTs versus the isoprenoid GDGT Crenarchaeol which is almost exclusively produced in the marine realm (Fig. S4)[18].

This index ranges from 0, representing no branched GDGT input, to 1, representing no Crenarchaeol input[18]. A study on the Congo fan found that in samples where BIT exceeded 0.3, SST estimates would be biased by >2°C[19]. However, the application of a threshold above which SST bias is likely to occur is locality dependent, as it depends on the difference between the 'TEX_{86}' value of terrestrially sourced isoprenoid GDGTs, and the TEX_{86} of the marine GDGTs[2]. Branched GDGTs are preferentially preserved over isoprenoid GDGTs during oxic degradation and can also be produced in a marine environment, particularly under anoxic conditions[20–22]. BIT and TEX_{86} values can be investigated to determine if they correlate, and a location specific threshold can be established if a correlation exists, or if substantial scatter occurs above a certain BIT threshold[23–25]. In the sites used in this study, no statistically significant correlation exists between TEX_{86} and BIT ($r=0.0937$ and $p=0.5016$ using the function 'surrogateCor' in 'astrochron'; Meyers, 2014), suggesting that terrestrially derived GDGTs are not biasing the record, even at moderate to high BIT values (Fig. S5). However, samples in the TEX_{86} dataset with BIT values above 0.5 are scattered, and so six samples with a BIT above this value have been excluded from TEX_{86} and TEX_{86}^{L}-based calibrations (Figure S2). BIT also shows no strong relationship with OPTiMAL SSTs ($r=0.1493$ and $p=0.0997$ using the function 'surrogateCor' in 'astrochron')[26], indicating BIT is not substantially impacting SSTs reconstructed by this calibration. Higher BIT values predominantly occur earlier in the Cenozoic, with Plio-Pleistocene samples from AND-1B usually showing very low BIT (Fig S4). BIT values increase during and immediately following the Eocene Oligocene Transition (EOT), interpreted as a marked increase in soil erosion rates during the development of the first continent-wide ice sheets (Fig. S4). Higher BIT values also occur during the Miocene Climate Optimum (MCO), suggesting a temporary return to relatively more chemical weathering with more active glaciofluvial transport from surface meltwater runoff[27]. During the Middle Miocene Climate Transition (MMCT), a colder climate led to a reduction in chemical weathering and very slow soil development, with soils at high elevations of the Transantarctic Mountains remaining dry and without a well-formed saturated active layer from 14 Ma[28]. BIT data is sparse in offshore cores, hampering our ability to characterise the shift to increasingly hyper-arid conditions using this proxy. However, by the Plio/Pleistocene, very low BIT values indicate the presence of a dominantly hyper-arid terrestrial environment (Fig. S4).

3) In methane-rich environments, archaeal GDGTs can also be produced in sediments post-deposition by methanotrophic archaea[29]. The methane index (MI) quantifies the relative contribution of methanotrophic-produced GDGTs to those produced in the water column by non-methanotrophic Thaumarcheaota, where values >0.3 indicate a significant contribution from a source other than normal marine sedimentation[29]. All samples in the Ross Sea GDGT compilation exhibit MI values below 0.3, although a trend from slightly higher MI to lower MI is observed across the Cenozoic (Fig. S6).

4) Methanogenic Euryarchaeota can also synthesise GDGT-0, and to a lesser extent GDGT-1, GDGT-2 and GDGT-3[30–33]. Most modern distributions of the common phyla of archaea around Antarctica are dominated by Thaumarchaeota, but Euryarchaeota does form a relatively large proportion of the archaeal community in Circumpolar Deepwater in the Ross Sea[16,21,34]. The impact of Euryarchaeota on a GDGT distribution is described using %GDGT-0, where values >67% indicate that a sample contains a substantial contribution from methanogenic sourced GDGTs[32]. In the Ross Sea TEX_{86} and TEX^{L}_{86}-based reconstructions, with the exception of three samples, %GDGT-0 remains below the 67% threshold whereby the contribution from methanogenic archaea can bias TEX_{86} reconstructed temperatures (Fig.

S6). These three samples have been excluded from TEX_{86} and TEX_{86}^{L}-based calibrations (Figure S2).

5) Different strains of archaea have been found to display variable TEX_{86} values, despite having been cultured at the same temperatures[35]. However, a linear relationship was found between the Ring Index (RI) and temperature across all strains of archaea in culture experiments[35] (Qin et al., 2015). The RI as defined by Zhang et al. (2016)[36] is used in this study, where higher values indicate warmer temperatures (Fig. S6). In the modern ocean, TEX_{86} and RI are correlated, and RI can be calculated from TEX_{86} using a regression[36]. If a sample's RI deviates from the calculated RI (ΔRI = [calculated RI] – [analysed RI]) enough that it does not lie within the 95% confidence interval of the modern regression (±0.3 ΔRI units), then the TEX_{86} value for that sample is considered to be potentially influenced by non-thermal factors and/or deviates from modern analogues (Fig. S6). These factors include the impact of GDGTs derived from soil, methanogenic and methanotrophic archaea as described above, or potentially other non-thermal impacts on GDGT biosynthesis such as archaeal growth rates[36]. In the Ross Sea TEX_{86} and TEX_{86}^{L}-based compilation, 52 data points with values which fall outside of a ±0.3 ΔRI range have been excluded from temperature reconstructions, the majority of which (32) occur in AND-1B. Over the course of the Cenozoic, a long-term trend from more positive ΔRI in the Eocene to more negative ΔRI in the Pliocene is observed (Fig. S6). Several high BIT values are associated with large deviations in ΔRI ($r=0.3929$, $p=0.0174$) (Fig. S7). A stronger relationship is found between MI and ΔRI, with higher values of MI correlating with larger positive deviations in ΔRI while lower values have more negative ΔRI deviations ($r=0.5856$, $p<0.0010$) (Fig. S7). The relationship is even stronger when ΔRI is compared to %GDGT-0 ($r=0.9017$, $p<0.0010$) indicating the abundance of GDGT-0 strongly influences whether a sample falls outside of a

±0.3 ΔRI range (Fig. S7). Changes in the ΔRI over the Cenozoic may therefore be driven by shifts in archaeal community composition. Culture and mesocosm studies show that different strains of archaea display variable TEX_{86}-growth temperature relationships[35,37]. Changing archaeal community composition in the Ross Sea could therefore compromise TEX_{86}-based temperature reconstructions as these methods apply a one-dimensional ratio across the total data set. OPTiMAL mitigates this issue by assessing GDGT distributions on a sample-by-sample basis, and using a multi-dimensional method to find the strongest temperature relationship between each sample and the modern calibration dataset, thereby also considering changes in GDGT-temperature relationships that result from shifts in archaeal communities[5].

S2. Temperature compilation

There are caveats to compiling a long-term record from multiple sites. In particular, depositional environments can vary greatly between sites, and within an individual record. Most of the sample localities were deposited in glacimarine settings, where marine conditions vary from ice-proximal to open water, with variable sea ice, melt water inputs and associated changes in water column stratification[38–41]. These factors could influence the GDGT distributions present, as there may be variation in archaeal communities, and depth of GDGT export, between different environments. By assessing the distribution in each sample individually and linking it back its nearest neighbours in the modern calibration dataset, OPTiMAL can take account of changing GDGT distributions through a core, which mitigates some of the impact of changing depositional environments,

While the focus of this study is long-term Cenozoic trends, superimposed on these trends are regular glacial/interglacial cycles. Hartman et al. (2018)[6] investigated temperature trends between glacials and interglacials in IODP U1356 and found an average temperature difference of 3.1°C. When these interglacial and glacial data are examined separately, comparable trends to the complete dataset are identified, indicating a late Oligocene cooling trend after 25 Ma is apparent across both interglacial and glacial periods. This also holds true when values are calibrated to OPTiMAL, with a 3.3°C difference between average glacial and interglacial values through the Oligocene, and both climate states showing cooler late Oligocene values (Fig. S8). Hartman et al. (2018)[6] were able to associate samples with glacial or interglacial intervals due to distinct lithological differences between cycles, driven by large biological productivity changes in the Southern Ocean as frontal systems migrated over the site[42]. However, there are some considerations when adopting this relationship for separating interglacial and glacial values within our Ross Sea compilation. In the ice proximal, continental shelf settings of AND-1B, AND-2A, CRP 2/2A and CIROS-1, glacial intervals are marked by ice overriding and deposition of sub-ice or grounding line proximal diamictites. This means that either no contemporaneous GDGTs are deposited (i.e. the site was ice covered rather than marine), or in the case of grounding line proximal sediments, there is an increased likelihood that GDGTs would reflect a reworked rather than contemporaneous distribution, as is the case for other biomarkers in these settings[43]. Sampling at these sites was therefore biased to interglacial or transitional periods when the sites were in a marine setting, and temperatures therefore predominantly reflect interglacial/transitional states. At the more ice-distal continental shelf setting of DSDP 270, bathymetric constraints preclude the migration of Southern Ocean frontal systems over the site, while its outer shelf setting results in glacial overriding being absent in most intervals. Consequently, lithological changes are more subtle and cannot be clearly associated with orbitally paced glacial or interglacial periods, like at IODP U1356 or the other Ross Sea sites in this compilation. While we cannot clearly ascribe samples to either a glacial or interglacial period in DSDP 270, it was sampled based on maintaining a relatively even sample spacing rather than targeting specific lithofacies, and we do not consider it likely that the late Oligocene cooling seen in this core is the result of a systematic shift whereby there was preferential sampling of interglacials earlier in the record (i.e. pre 24.5 Ma), and glacials later in the record (i.e. post 24.5Ma). This assumption that the cooling signal post-24 Ma in DSDP 270 is not a function of a sampling bias is also supported by cool temperatures in CRP 2/2A and CIROS-1, which as discussed above are inherently skewed toward interglacial values. In addition, CIROS-1 values between 23.3 and ~22.8 Ma, are consistent with coeval DSDP 270 values indicating the post 24 Ma cooling is a regional signal throughout the Ross Sea. Finally, this inference of sustained regional cooling through this interval is also supported by numerous paleoenvironmental indicators from both the Ross Sea and Wilkes Land, as outlined in the main text and Table S1. It is likely that glacial/interglacial variability in the Ross Sea is less than that from IODP U1356 offshore Wilkes Land, as IODP U1356 is an open ocean site near a dynamic oceanic frontal boundary[44], across which there is currently a temperature gradient of ~5°C (Fig. 1). The magnitude of late Oligocene cooling in the Ross Sea is ~3.5°C (i.e. cooling from an average of ~7°C at 25 Ma to 3.5°C at 24 Ma). This is therefore larger than what would be expected for average glacial/interglacial variability in the Ross Sea, based on 3.3°C variability at U1356.

Other biomarkers in the Ross Sea region display a variable contribution from reworked material, particularly in more ice-proximal depositional environments[43]. GDGTs have only been identified in sediments as old as the Jurassic[45,46], and degrade with thermal maturation of sediments[2,47]. It is therefore considered unlikely that GDGTs have been reworked from the predominately Permian-Triassic and variably thermally matured sedimentary rocks in the Ross Sea region[48], but it is possible that GDGTs from earlier Cenozoic rift-fill sediments could be incorporated into younger material. DSDP 270 reflects an ice distal depositional setting, with the exception of a short interval of glacial proximity, and has been found to contain very little evidence for a reworked contribution to biomarker distributions or microfossil assemblages[43]. At other sites, potential reworking could explain some of the large nearest neighbour values and ΔRI deviations, as the GDGT distribution could be reflecting a mixed source (i.e. derived from both contemporaneous and reworked material). Reworking may also account for samples which display markedly different temperatures than adjacent samples. However, the agreement between GDGT-based temperatures and paleoenvironmental information (S1) suggests that the impact of any reworked GDGT contribution is minimal.

Age	Ross Sea OPTiMAL SST	Wilkes Land OPTiMAL SST	Other paleoenvironmental information
late Pliocene (Post PWP) – Pleistocene (3-0 Ma)	2.6 ± 2.7	-	Cold temperatures of 0-2°C are coincident with decreasing CO_2, cooler bottom water temperatures, expanded Antarctic sea ice, and increased global ice volume with the intensification of Northern Hemisphere Ice Sheets[40,49–51].
early Pliocene – PWP (5.33-3 Ma)	6.1 ± 2.0	-	Global SST reconstructions from models and data imply a global average anomaly of +2-3°C from present with 2-3 times temperature amplification at the poles[52,53]. Sedimentary facies and microfossil assemblages from AND-1B support a relatively warm climate, with evidence for markedly reduced WAIS and sea ice extent, and the presence of Subantarctic diatoms[40,54]. Sedimentary facies indicate enhanced meltwater processes at the margins of the AIS, especially during glacial advance and retreat[40,55]. Increased meltwater input, including that of seasonal sea ice melt, can greatly enhance thermal stratification of the water column, leading to warmer SSTs during the periods of meltwater release[9,40].
MMCT- late Miocene (14.5-5.33 Ma)	2.4 ± 0.8	2.6 ± 1.2	Large unconformities in drill cores from around Antarctica are associated with significant marine-based ice sheet advance onto Antarctica's continental shelf[7,43,56–58]. Reduction in chemical weathering and very slow soil development onshore, with soils at high elevations of the Transantarctic Mountains remaining dry and without a well-formed saturated active layer from 14 Ma[28]. Breakdown in gradient between Wilkes Land and the Ross Sea suggests a movement or intensification of the Antarctic Divergence to a position north of U1356A, similar to today's oceanographic configuration, with U1356 becoming more heavily influenced by cold Antarctic Surface Water forming in the Ross Sea and being advected to Wilkes Land via the easterly Antarctic Slope Current[7].
MCO (17-14.5 Ma)	2.2 ± 1.6	7.4 ± 3.8	SST model estimates indicate ~0 to 5°C for high southern latitudes[59]. Anomaly from present of ~4-5°C from planktic foraminiferal Mg/Ca on two subantarctic core sites[60]. Mean summer temperatures of ~5°C in the Dry Valleys indicated by ostracode and beetle fossils[61]. Δ_{47} clumped isotopes from molluscs (max temperature of ~10°C) and leaf wax isotopes in AND-2A support the MCO as a period of highly variable conditions, including a prolonged period of warmth between ~16.7 and 14.6 Ma, when vegetation increased onshore and the ice sheet likely retreated inland[41,62,63]. BIT values in offshore cores (this study), and geomorphology from the Dry Valleys suggest a temporary return to more chemical weathering and active glaciofluvial transport from surface meltwater runoff[27]. Significant temperature gradient still apparent between Wilkes Land and the Ross Sea. Although water mass exchange through the Tasmanian Gateway was operating at this time, this gradient is attributed to IODP U1356 being influenced by a weakening and/or more southerly location of the major Southern Ocean frontal systems[7].
early Miocene – MCO (23.01-17 Ma)	3.2 ± 1.4	-	Orbitally paced warmer and cooler climate states supported by sedimentology, physical properties, chemical weathering indices, and marine and terrestrial microfossils in AND-2A[41].
late Oligocene (28.1-23.01 Ma)	3.8 ± 2.2	9.4 ± 4.9	Warm conditions between 25 and 26 Ma following Oi-1b from nannofossil assemblages on Maud Rise and Kerguelen Plateau[64], and dinocysts, pollen assemblages and a lack of IRD offshore Wilkes Land[42,65].

			Following 25 Ma temperatures and dinocysts indicate cooling and the presence of sea ice offshore Wilkes Land[6,65]. Dynamic proto-Antarctic Circumpolar Current fluctuated in intensity and position offshore Wilkes Land between 24.2 Ma and Mi-1[44]. Temperature gradient between the Ross Sea and Wilkes Land, and the presence of warmer, oligotrophic dinoflagellates in IODP U1356 suggest IODP U1356 was still influenced by lower latitude water masses during the late Oligocene[65]. Offshore Cape Adare (DSDP 274) warm, oligotrophic sea surface conditions existed through the Oligocene, with peak warmth at ~26.5 Ma[66]. Cool-water nannofossil, foraminiferal and marine macrofossil assemblages in the Ross Sea[67–70]. Long-term cooling and drying trend from palynology, facies analysis, clay mineral and chemical weathering indices Cape Roberts Project cores from the western Ross Sea[71–75]. Orbitally paced marine grounding of EAIS outlet glaciers at the margins of the western Ross Sea[38,76,77].
early Oligocene (33.9-28.1 Ma)	4.5 ± 1.3	13.5 ± 4.7	EOT: Ross Sea temperatures as low as 2.4°C coincide with an increase in sea-ice faunal markers Protoperidinaceae in IODP U1356A from the Wilkes Land margin and model simulations suggesting the development of extensive sea ice around Antarctica[78–80]. A ~5°C cooling in other high to mid-southern latitude sites[81]. BIT values (this study) increase during and immediately following the EOT, interpreted as a marked increase in soil erosion rates during the development of the first continent-wide ice sheets. Early Oligocene temperature gradient between Ross Sea and Wilkes Land is consistent with proxy data-model comparisons that indicate during the early phases of the tectonic opening of the Tasmanian oceanic gateway, Wilkes Land maintained a stronger influence of warmer water from lower latitudes via the Leeuwin Current, whereas the large, cool, Ross Sea gyre restricted warm low-latitude water masses penetrating further south[79,82].
late Eocene (37.8-33.9 Ma)	5.2 ± 1.8	-	Increase in high latitude radiolarian fauna at Priabonian Oxygen Isotope Maximum (37.3 Ma) in DSDP 277[83]. A shift in Nd isotopes on the Kerguelen Plateau is inferred to represent a period of iceberg calving and enhanced erosion during Priabonian Oxygen Isotope Maximum[84]. Iceberg calving in the South Atlantic from 36.5 Ma[85]. Cool, temperate vegetation and periodic glaciation from 35.8 Ma in Prydz Bay[86,87]. Cool, temperate vegetation at the Cape Roberts Project site from 34 Ma[88].
middle Eocene (47.8-37.8 Ma)	9.7 ± 2.8	-	Temperate vegetation and warm, temperate waters in the Ross Sea region indicated by pollen, molluscs, crocodile tooth in McMurdo Erratics[89–91]. Temperate rainforest, MATs of 14±3°C in Wilkes Land[92].

Supplementary Table 1: Average OPTiMAL temperatures for timeslices in the Ross Sea and Wilkes Land, and comparisons to other paleoenvironmental information. PWP: Pliocene Warm Period, MMCT: Middle Miocene Climate Transition, MCO: Miocene Climate Optimum.

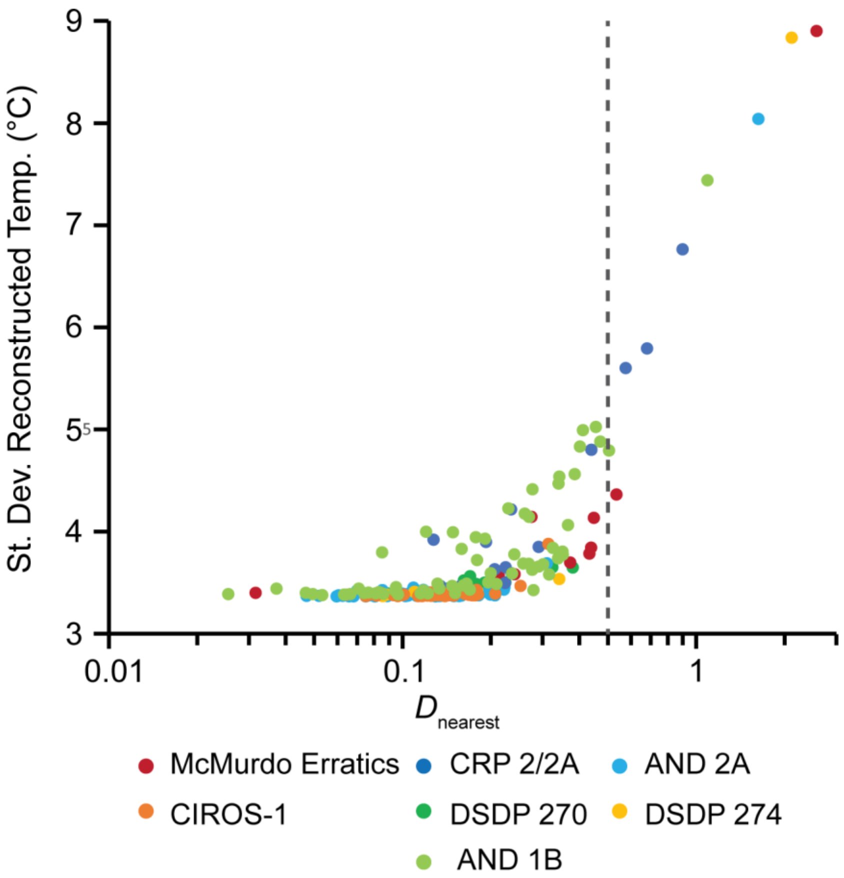

Figure S1. Standard deviations of reconstructed OPTiMAL temperatures, compared to nearest neighbour values ($D_{nearest}$). Samples with $D_{nearest}$ > 0.5 are unlikely to be well constrained by any current calibration model[5].

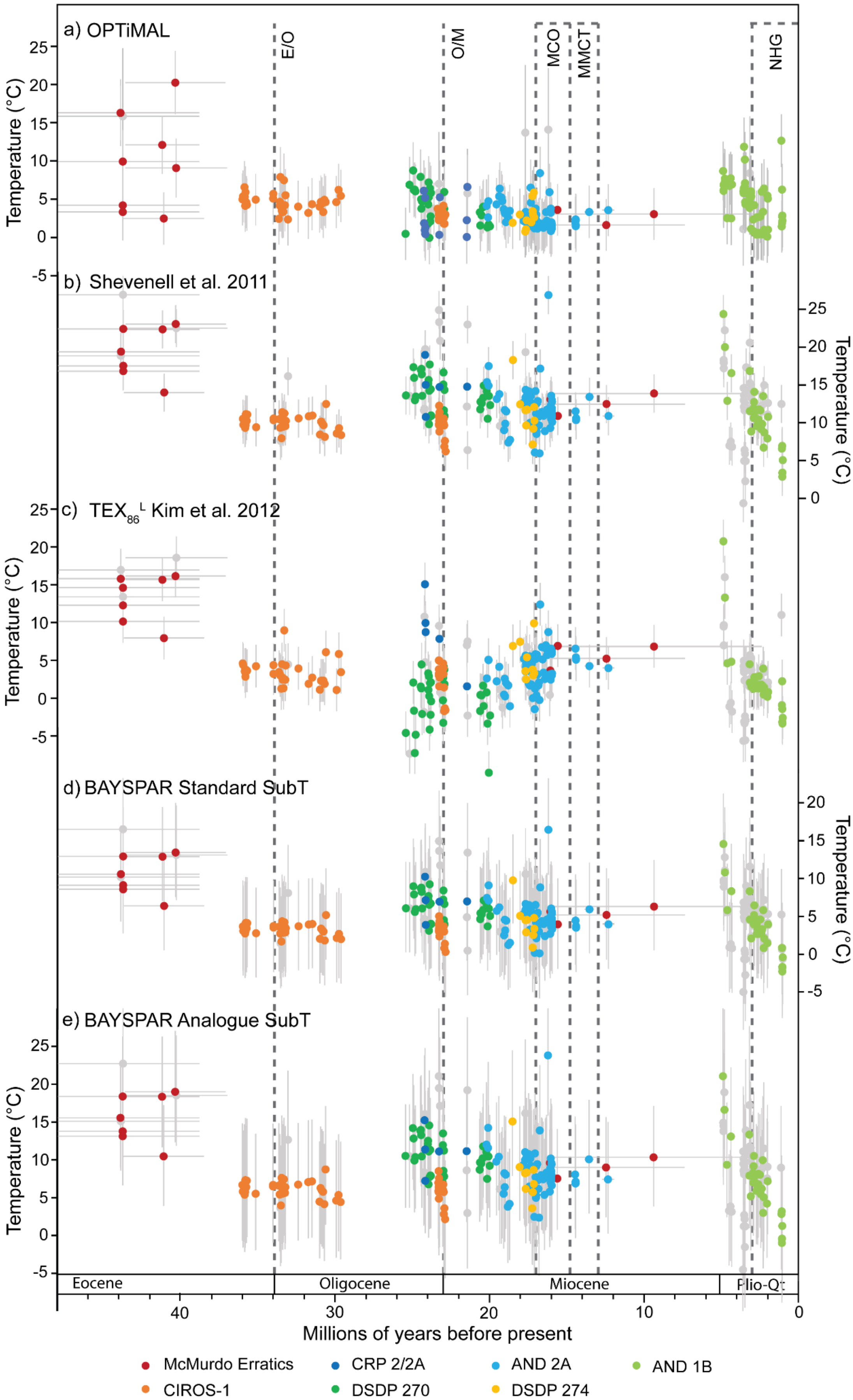

a) OPTiMAL
b) Shevenell et al. 2011
c) TEX$_{86}^{L}$ Kim et al. 2012
d) BAYSPAR Standard SubT
e) BAYSPAR Analogue SubT
E/O
O/M
MCO
MMCT
NHG
Temperature (°C)
Eocene
Oligocene
Miocene
Plio-Qt
Millions of years before present
McMurdo Erratics
CIROS-1
CRP 2/2A
DSDP 270
AND 2A
DSDP 274
AND 1B

Figure S2. OPTiMAL, TEX_{86} and TEX_{86}^{L} temperature calibrations suitable for high latitude use, applied to Ross Sea sample sites through the Cenozoic. a)OPTiMAL[5] (standard deviation of 3.61°C), b) Shevenell et al. (2011)[9](standard error of ±2.5°C), b) TEX_{86}^{L} Kim et al. (2012)[12] (error of ±2.8°C), c) BAYSPAR Standard SubT[10,11], and d) BAYSPAR Analogue SubT[10,11](errors displayed are 90th percentile confidence intervals). Grey samples indicate samples which failed screening measure to identify non-analogue samples and as such have been removed from the compilation. Dashed bars indicate significant climate events; E/O= Eocene/Oligocene boundary, O/M= Oligocene/Miocene boundary, MCO= Miocene Climate Optimum, MMCT= Mid-Miocene Climate Transition, NHG= Northern Hemisphere glaciation.

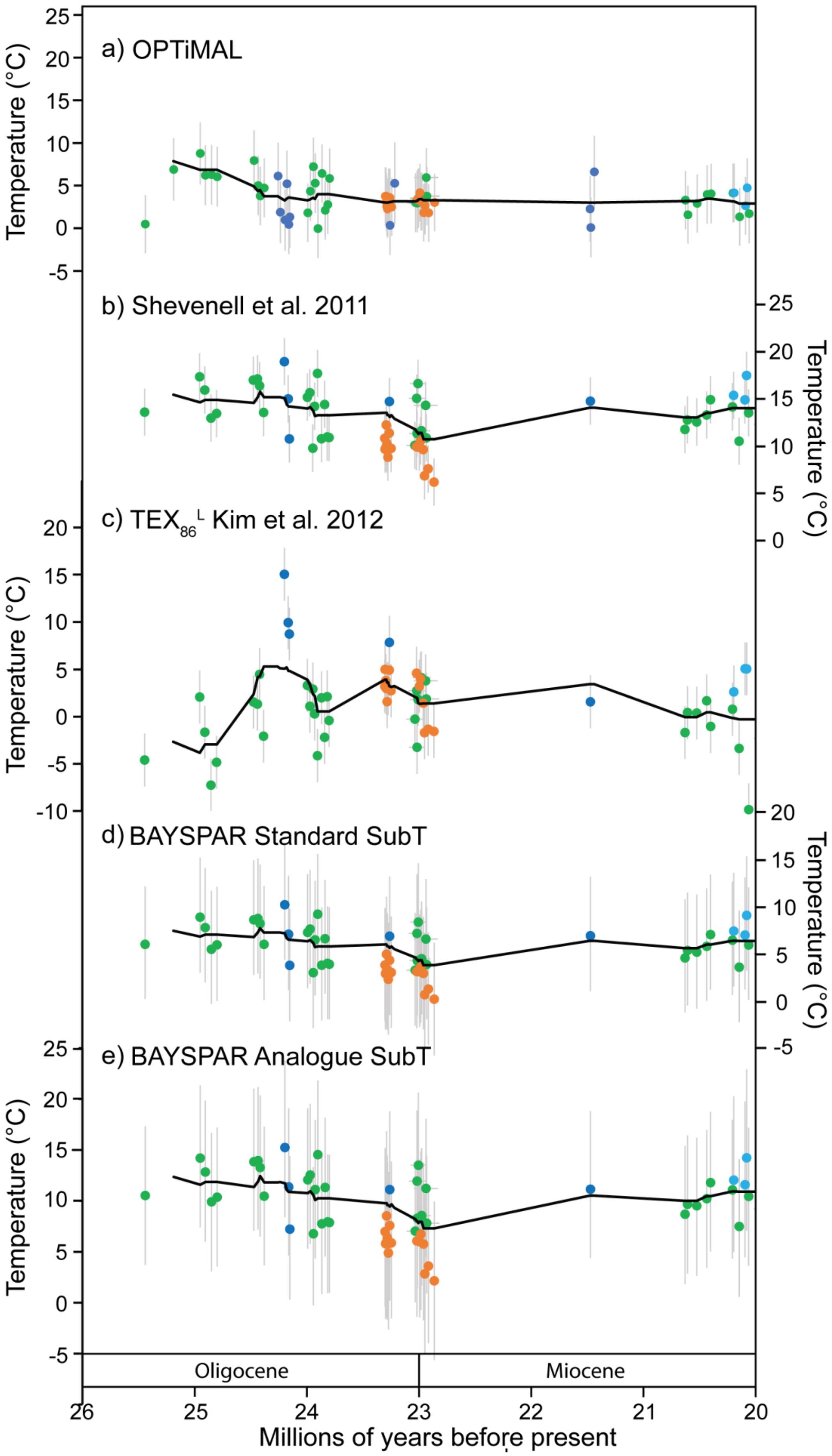
a) OPTiMAL
b) Shevenell et al. 2011
c) TEX$_{86}^{L}$ Kim et al. 2012
d) BAYSPAR Standard SubT
e) BAYSPAR Analogue SubT
Temperature (°C)
Oligocene
Miocene
Millions of years before present

Figure S3: OPTiMAL, TEX$_{86}$ *and* TEX_{86}^{L} *temperature calibrations suitable for high latitude use, applied to the late Oligocene/early Miocene interval of the compilation. a)OPTiMAL*[5] *(standard deviation of 3.61°C), b) Shevenell et al. (2011)*[9]*(standard error of ±2.5°C), b)* TEX_{86}^{L} *Kim et al. (2012)*[12] *(error of ±2.8°C), c) BAYSPAR Standard SubT*[10,11]*, and d) BAYSPAR Analogue SubT*[10,11]*(errors displayed are 90*th *percentile confidence intervals). Black lines represent a 500 kyr moving average.*

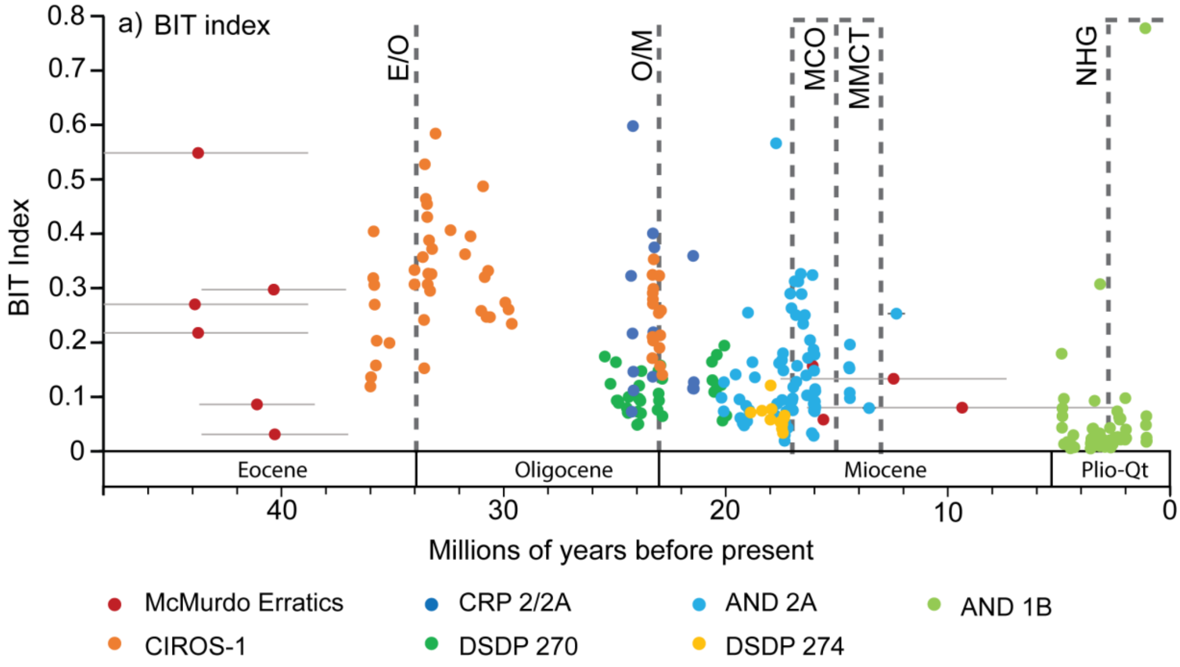

Figure S4. a) BIT index for Ross Sea sample sites through the Cenozoic. Dashed bars indicate significant climate events; E/O= Eocene/Oligocene boundary, O/M= Oligocene/Miocene boundary, MCO= Miocene Climate Optimum, MMCT= Mid-Miocene Climate Transition, NHG= Northern Hemisphere glaciation.

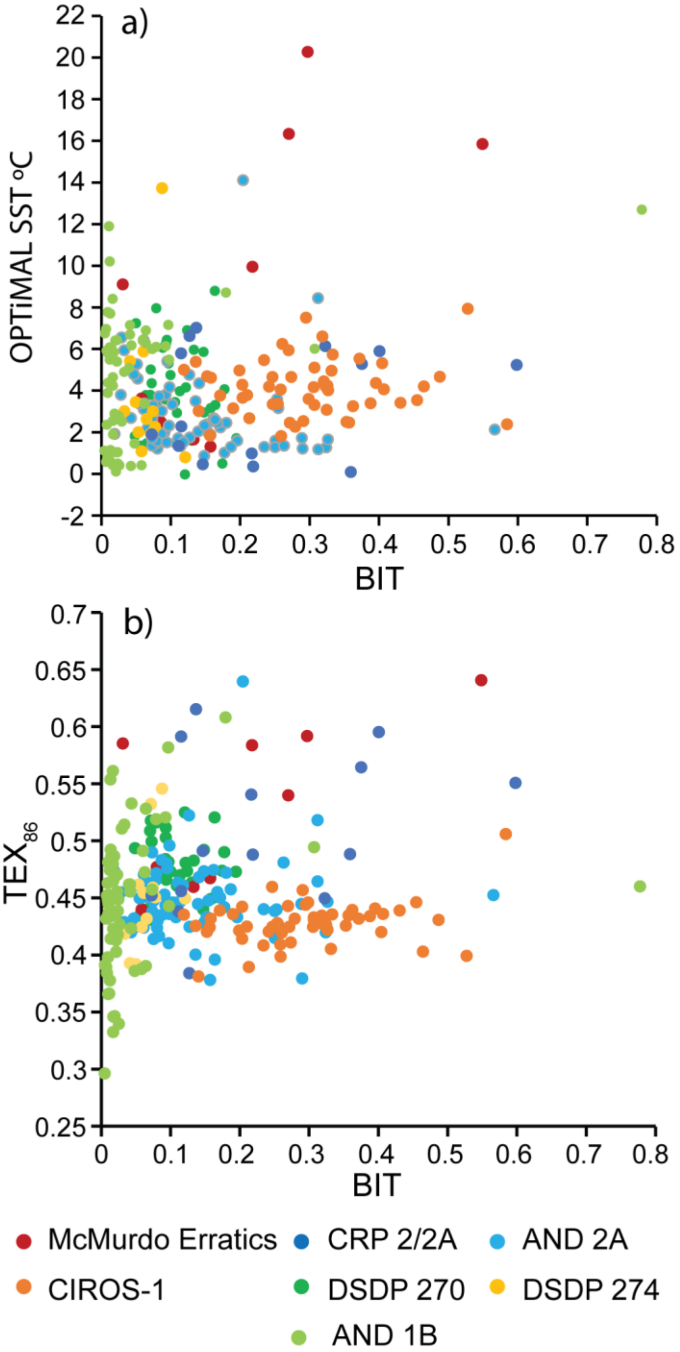

Figure S5. Scatter plots of a) BIT and OPTiMAL SST (r=0.1493, p=0.0997) and b) BIT and TEX_{86} (r=0.0937, p=0.5016) in Ross Sea sample sites.

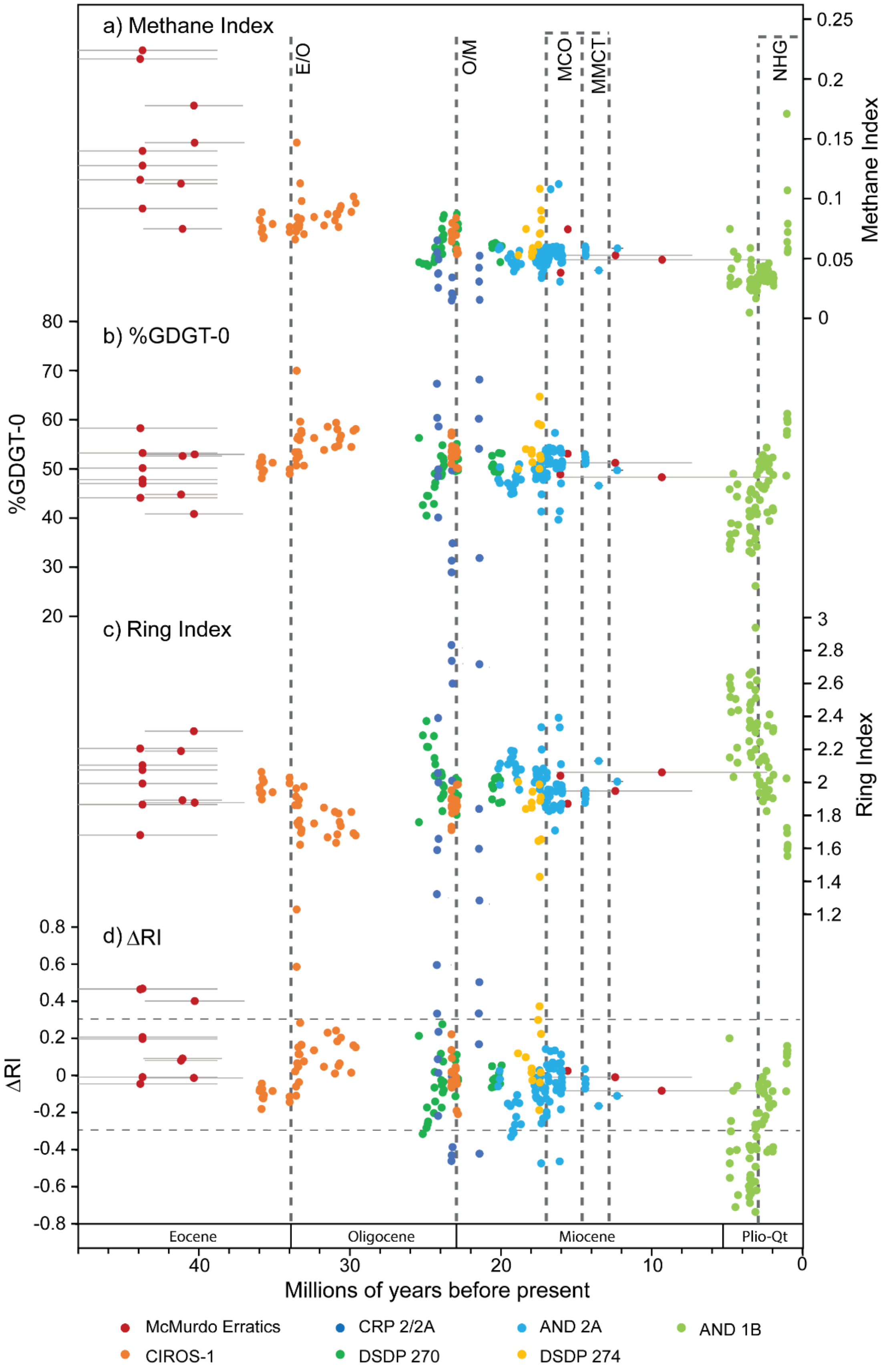

a) Methane Index
b) %GDGT-0
c) Ring Index
d) ΔRI
E/O
O/M
MCO
MMCT
NHG
Methane Index
%GDGT-0
Ring Index
ΔRI
0.25
0.2
0.15
0.1
0.05
0
80
70
60
50
40
30
20
3
2.8
2.6
2.4
2.2
2
1.8
1.6
1.4
1.2
0.8
0.6
0.4
0.2
0
-0.2
-0.4
-0.6
-0.8
Eocene
Oligocene
Miocene
Plio-Qt
40
30
20
10
0
Millions of years before present
McMurdo Erratics
CIROS-1
CRP 2/2A
DSDP 270
AND 2A
DSDP 274
AND 1B

Figure S6. a) Methane Index, b) %GDGT-0, c) Ring Index and d) ΔRI values for Ross Sea sample sites through the Cenozoic. Dashed lines on d) represent the 95% confidence interval of the modern TEX_{86}*-RI regression*[36]*. Vertical dashed bars indicate significant climate events; E/O= Eocene/Oligocene boundary, O/M= Oligocene/Miocene boundary, MCO= Miocene Climate Optimum, MMCT= Mid-Miocene Climate Transition, NHG= Northern Hemisphere glaciation.*

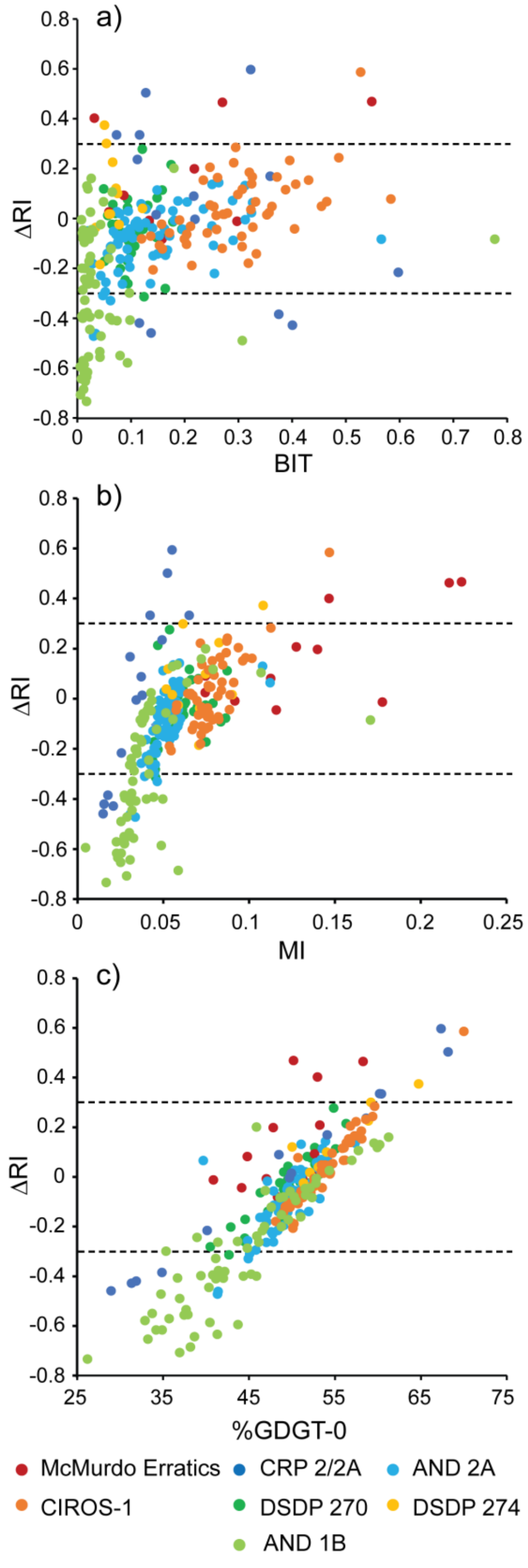

Figure S7. Scatter plots of a) ΔRI and BIT (r=0.3929, p=0.0174), b) ΔRI and MI (r=0.5856, p<0.0010), and c) ΔRI and %GDGT-0 (r=0.9017, p<0.0010). Dashed lines represent the 95% confidence interval of the modern TEX_{86}-RI regression[36].

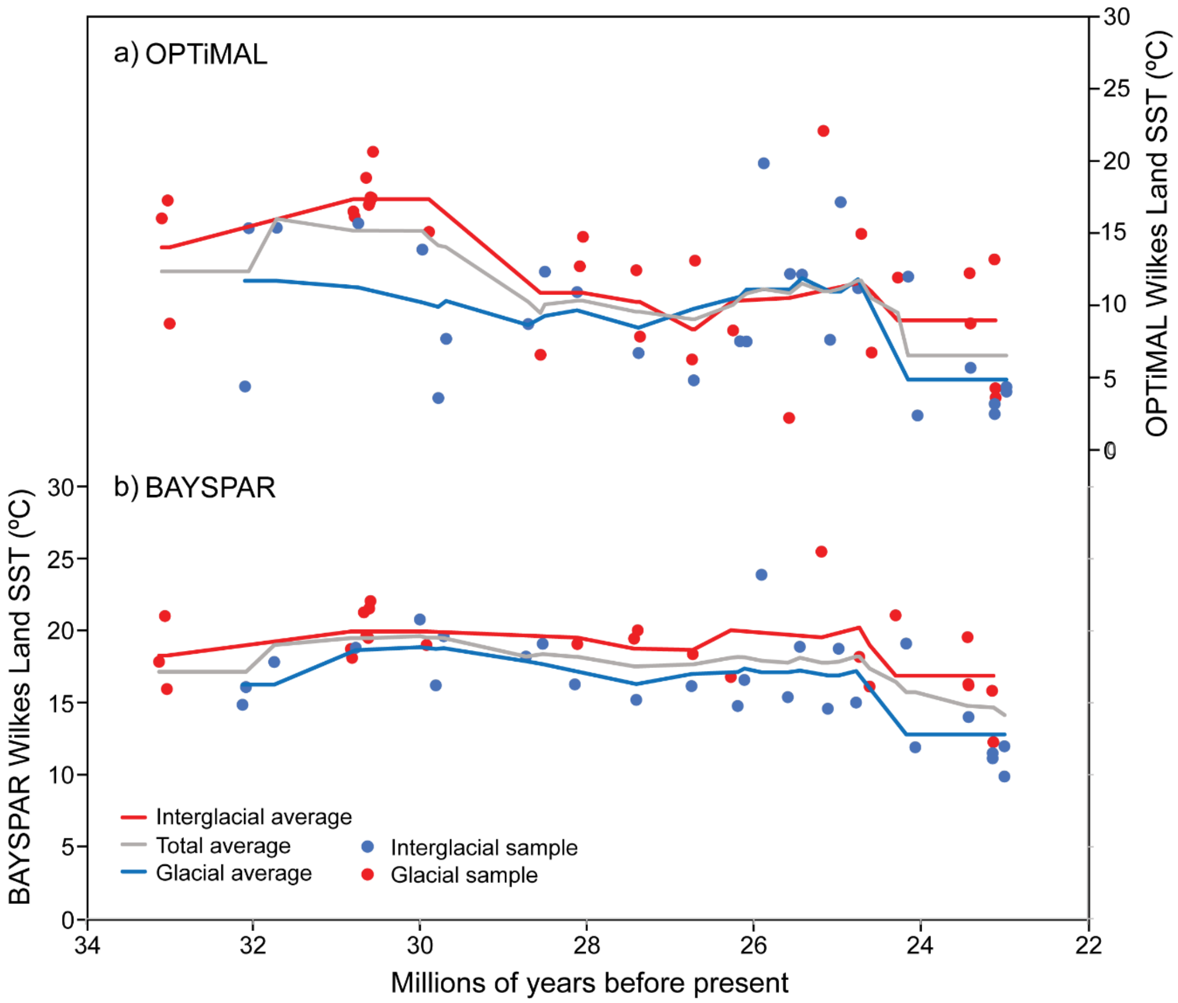

Figure S8. Comparison of interglacial and glacial trends for site U1356, Wilkes Land, using a 2.5 myr moving average to account for larger sample spacing when samples are separated into glacial and interglacial values. OPTiMAL includes more data than the BAYSPAR TEX$_{86}$-based method, as it uses a different method (nearest neighbour values) to identify non-analogue samples.

Supplementary references

1. Schouten, S., Hopmans, E. C., Schefuß, E. & Sinninghe Damsté, J. S. Distributional variations in marine crenarchaeotal membrane lipids: a new tool for reconstructing ancient sea water temperatures? *Earth and Planetary Science Letters* **204**, 265–274 (2002).
2. Schouten, S., Hopmans, E. C. & Sinninghe Damsté, J. S. The organic geochemistry of glycerol dialkyl glycerol tetraether lipids: A review. *Organic Geochemistry* **54**, 19–61 (2013).
3. Kim, J.-H., Schouten, S., Hopmans, E. C., Donner, B. & Sinninghe Damsté, J. S. Global sediment core-top calibration of the TEX_{86} paleothermometer in the ocean. *Geochimica et Cosmochimica Acta* **72**, 1154–1173 (2008).
4. Fietz, S., Ho, S. L., Huguet, C., Rosell-Melé, A. & Martínez-García, A. Appraising GDGT-based seawater temperature indices in the Southern Ocean. *Organic Geochemistry* **102**, 93–105 (2016).
5. Dunkley Jones, T. *et al.* OPTiMAL: a new machine learning approach for GDGT-based palaeothermometry. *Climate of the Past* **16**, 2599–2617 (2020).
6. Hartman, J. D. *et al.* Paleoceanography and ice sheet variability offshore Wilkes Land, Antarctica – Part 3: Insights from Oligocene–Miocene TEX_{86}-based sea surface temperature reconstructions. *Climate of the Past* **14**, 1275–1297 (2018).
7. Sangiorgi, F. *et al.* Southern Ocean warming and Wilkes Land ice sheet retreat during the mid-Miocene. *Nature Communications* **9**, 317 (2018).
8. Kim, J.-H. *et al.* New indices and calibrations derived from the distribution of crenarchaeal isoprenoid tetraether lipids: Implications for past sea surface temperature reconstructions. *Geochimica et Cosmochimica Acta* **74**, 4639–4654 (2010).

9. Shevenell, A. E., Ingalls, A. E., Domack, E. W. & Kelly, C. Holocene Southern Ocean surface temperature variability west of the Antarctic Peninsula. *Nature* **470**, 250–254 (2011).

10. Tierney, J. E. & Tingley, M. P. A Bayesian, spatially-varying calibration model for the TEX_{86} proxy. *Geochimica et Cosmochimica Acta* **127**, 83–106 (2014).

11. Tierney, J. E. & Tingley, M. P. A TEX_{86} surface sediment database and extended Bayesian calibration. *Scientific Data* **2**, (2015).

12. Kim, J.-H. *et al.* Holocene subsurface temperature variability in the eastern Antarctic continental margin. *Geophys. Res. Lett.* **39**, L06705 (2012).

13. Taylor, K. W. R., Huber, M., Hollis, C. J., Hernandez-Sanchez, M. T. & Pancost, R. D. Re-evaluating modern and Palaeogene GDGT distributions: Implications for SST reconstructions. *Global and Planetary Change* **108**, 158–174 (2013).

14. Massana, R. *et al.* Vertical distribution and temporal variation of marine planktonic archaea in the Gerlache Strait, Antarctica, during early spring. *Limnology and Oceanography* **43**, 607–617 (1998).

15. Murray, A. E. *et al.* Seasonal and spatial variability of bacterial and archaeal assemblages in the coastal waters near Anvers Island, Antarctica. *Applied and Environmental Microbiology* **64**, 2585–2595 (1998).

16. Church, M. J. *et al.* Abundance and distribution of planktonic Archaea and Bacteria in the waters west of the Antarctic Peninsula. *Limnology and Oceanography* **48**, 1893–1902 (2003).

17. Kalanetra, K. M., Bano, N. & Hollibaugh, J. T. Ammonia-oxidizing archaea in the arctic ocean and antarctic coastal waters. *Environmental Microbiology* **11**, 2434–2445 (2009).

18. Hopmans, E. C. *et al.* A novel proxy for terrestrial organic matter in sediments based on branched and isoprenoid tetraether lipids. *Earth and Planetary Science Letters* **224**, 107–116 (2004).

19. Weijers, J. W. H., Schouten, S., Spaargaren, O. C. & Sinninghe Damsté, J. S. Occurrence and distribution of tetraether membrane lipids in soils: Implications for the use of the TEX_{86} proxy and the BIT index. *Organic Geochemistry* **37**, 1680–1693 (2006).

20. Huguet, C. *et al.* Selective preservation of soil organic matter in oxidized marine sediments (Madeira Abyssal Plain). *Geochimica et Cosmochimica Acta* **72**, 6061–6068 (2008).

21. Weijers, J. W. H., Schefuß, E., Kim, J.-H., Sinninghe Damsté, J. S. & Schouten, S. Constraints on the sources of branched tetraether membrane lipids in distal marine sediments. *Organic Geochemistry* **72**, 14–22 (2014).

22. Xiao, W. *et al.* Ubiquitous production of branched glycerol dialkyl glycerol tetraethers (brGDGTs) in global marine environments: A new source indicator for brGDGTs. *Biogeosciences* **13**, 5883–5894 (2016).

23. Schouten, S. *et al.* An interlaboratory study of TEX_{86} and BIT analysis using high-performance liquid chromatography–mass spectrometry. *Geochem. Geophys. Geosyst.* **10**, 13 PP. (2009).

24. Bijl, P. K. *et al.* Eocene cooling linked to early flow across the Tasmanian Gateway. *PNAS* (2013) doi:10.1073/pnas.1220872110.

25. Schouten, S. *et al.* An interlaboratory study of TEX_{86} and BIT analysis of sediments, extracts, and standard mixtures. *Geochemistry, Geophysics, Geosystems* **14**, 5263–5285 (2013).

26. Meyers, S., Malinverno, A., Hinnov, L., Zeeden, C. & Moron, V. *astrochron: A Computational Tool for Astrochronology*. (2019).

27. Lewis, A. R., Marchant, D. R., Kowalewski, D. E., Baldwin, S. L. & Webb, L. E. The age and origin of the Labyrinth, western Dry Valleys, Antarctica: Evidence for extensive middle Miocene subglacial floods and freshwater discharge to the Southern Ocean. *Geology* **34**, 513–516 (2006).

28. Lewis, A. R., Marchant, D. R., Ashworth, A. C., Hemming, S. R. & Machlus, M. L. Major middle Miocene global climate change: Evidence from East Antarctica and the Transantarctic Mountains. *Geological Society of America Bulletin* **119**, 1449–1461 (2007).

29. Zhang, Y. G. *et al.* Methane Index: A tetraether archaeal lipid biomarker indicator for detecting the instability of marine gas hydrates. *Earth and Planetary Science Letters* **307**, 525–534 (2011).

30. Pancost, R. D., Hopmans, E. C. & Sinninghe Damsté, J. S. Archaeal lipids in mediterranean cold seeps: Molecular proxies for anaerobic methane oxidation. *Geochimica et Cosmochimica Acta* **65**, 1611–1627 (2001).

31. Blaga, C. I., Reichart, G.-J., Heiri, O. & Sinninghe Damsté, J. S. Tetraether membrane lipid distributions in water-column particulate matter and sediments: A study of 47 European lakes along a north-south transect. *Journal of Paleolimnology* **41**, 523–540 (2009).

32. Sinninghe Damsté, J. S., Ossebaar, J., Schouten, S. & Verschuren, D. Distribution of tetraether lipids in the 25-ka sedimentary record of Lake Challa: Extracting reliable TEX_{86} and MBT/CBT palaeotemperatures from an equatorial African lake. *Quaternary Science Reviews* **50**, 43–54 (2012).

33. Inglis, G. N. *et al.* Descent toward the Icehouse: Eocene sea surface cooling inferred from GDGT distributions. *Paleoceanography* **30**, 1000–1020 (2015).

34. Alonso-Sáez, L., Andersson, A., Heinrich, F. & Bertilsson, S. High archaeal diversity in Antarctic circumpolar deep waters. *Environmental Microbiology Reports* **3**, 689–697 (2011).

35. Qin, W. *et al.* Confounding effects of oxygen and temperature on the TEX_{86} signature of marine Thaumarchaeota. *Proceedings of the National Academy of Sciences of the United States of America* **112**, 10979–10984 (2015).

36. Zhang, Y. G., Pagani, M. & Wang, Z. Ring Index: A new strategy to evaluate the integrity of TEX_{86} paleothermometry. *Paleoceanography* **31**, 220–232 (2016).

37. Elling, F. J., Könneke, M., Mußmann, M., Greve, A. & Hinrichs, K.-U. Influence of temperature, pH, and salinity on membrane lipid composition and TEX_{86} of marine planktonic thaumarchaeal isolates. *Geochimica et Cosmochimica Acta* **171**, 238–255 (2015).

38. Hambrey, M. J., Barrett, P. J. & Robinson, P. H. Stratigraphy. *Antarctic Cenozoic History from the CIROS-1 drillhole, McMurdo Sound* **245**, 23–48 (1989).

39. Naish, T. R. *et al.* Sedimentary cyclicity in CRP drillcore, Victoria Land Basin, Antarctica. *Terra Antarctica* **8**, 225–244 (2001).

40. McKay, R. *et al.* Antarctic and Southern Ocean influences on Late Pliocene global cooling. *PNAS* **109**, 6423–6428 (2012).

41. Levy, R. *et al.* Antarctic ice sheet sensitivity to atmospheric CO_2 variations in the early to mid-Miocene. *Proceedings of the National Academy of Sciences of the United States of America* **113**, 3453–3458 (2016).

42. Salabarnada, A. *et al.* Paleoceanography and ice sheet variability offshore Wilkes Land, Antarctica - Part 1: Insights from late Oligocene astronomically paced contourite sedimentation. *Climate of the Past* **14**, 991–1014 (2018).

43. Duncan, B. *et al.* Lipid biomarker distributions in Oligocene and Miocene sediments from the Ross Sea region, Antarctica: Implications for use of biomarker proxies in glacially-influenced settings. *Palaeogeography, Palaeoclimatology, Palaeoecology* **516**, 71–89 (2019).

44. Evangelinos, D. *et al.* Late Oligocene-Miocene proto-Antarctic Circumpolar Current dynamics off the Wilkes Land margin, East Antarctica. *Global and Planetary Change* **191**, 103221 (2020).

45. Jenkyns, H. C., Schouten-Huibers, L., Schouten, S. & Sinninghe Damsté, J. S. Warm Middle Jurassic-Early Cretaceous high-latitude sea-surface temperatures from the Southern Ocean. *Climate of the Past* **8**, 215–225 (2012).

46. Robinson, S. A. *et al.* Early Jurassic North Atlantic sea-surface temperatures from TEX_{86} palaeothermometry. *Sedimentology* **64**, 215–230 (2017).

47. Schouten, S., Hopmans, E. C. & Sinninghe Damsté, J. S. The effect of maturity and depositional redox conditions on archaeal tetraether lipid palaeothermometry. *Organic Geochemistry* **35**, 567–571 (2004).

48. Barrett, P. J. History of the Ross Sea region during the deposition of the Beacon Supergroup 400 - 180 million years ago. *Journal of the Royal Society of New Zealand* **11**, 447–458 (1981).

49. Sosdian, S. & Rosenthal, Y. Deep-Sea Temperature and Ice Volume Changes Across the Pliocene-Pleistocene Climate Transitions. *Science* **325**, 306–310 (2009).

50. Bartoli, G., Hönisch, B. & Zeebe, R. E. Atmospheric CO_2 decline during the Pliocene intensification of Northern Hemisphere glaciations. *Paleoceanography* **26**, PA4213 (2011).

51. Haug, G. H. *et al.* North Pacific seasonality and the glaciation of North America 2.7 million years ago. *Nature* **433**, 821–825 (2005).

52. Masson-Delmotte, V. *et al.* Information from paleoclimate archives. *Climate change* 383–464 (2013).

53. Haywood, A. M., Dowsett, H. J. & Dolan, A. M. Integrating geological archives and climate models for the mid-Pliocene warm period. *Nature Communications* **7**, 10646 (2016).

54. Naish, T. *et al.* Obliquity-paced Pliocene West Antarctic ice sheet oscillations. *Nature* **458**, 322–328 (2009).

55. McKay, R. *et al.* The stratigraphic signature of the late Cenozoic Antarctic Ice Sheets in the Ross Embayment. *Bulletin of the Geological Society of America* **121**, 1537–1561 (2009).

56. De Santis, L., Prato, S., Brancolini, G., Lovo, M. & Torelli, L. The Eastern Ross Sea continental shelf during the Cenozoic: implications for the West Antarctic ice sheet development. *Global and Planetary Change* **23**, 173–196 (1999).

57. Colleoni, F. *et al.* Past continental shelf evolution increased Antarctic ice sheet sensitivity to climatic conditions. *Sci Rep* **8**, (2018).

58. Levy, R. H. *et al.* Antarctic ice-sheet sensitivity to obliquity forcing enhanced through ocean connections. *Nature Geoscience* 1 (2019) doi:10.1038/s41561-018-0284-4.

59. You, Y., Huber, M., Müller, R. D., Poulsen, C. J. & Ribbe, J. Simulation of the Middle Miocene Climate Optimum. *Geophysical Research Letters* **36**, n/a-n/a (2009).

60. Shevenell, A. E., Kennett, J. P. & Lea, D. W. Middle Miocene Southern Ocean Cooling and Antarctic Cryosphere Expansion. *Science* **305**, 1766–1770 (2004).

61. Lewis, A. R. *et al.* Mid-Miocene cooling and the extinction of tundra in continental Antarctica. *Proceedings of the National Academy of Sciences of the United States of America* **105**, 10676–10680 (2008).

62. Warny, S. *et al.* Palynomorphs from a sediment core reveal a sudden remarkably warm Antarctica during the middle Miocene. *Geology* **37**, 955–958 (2009).

63. Feakins, S. J., Warny, S. & Lee, J.-E. Hydrologic cycling over Antarctica during the middle Miocene warming. *Nature Geosci* **5**, 557–560 (2012).

64. Villa, G. & Persico, D. Late Oligocene climatic changes: Evidence from calcareous nannofossils at Kerguelen Plateau Site 748 (Southern Ocean). *Palaeogeography, Palaeoclimatology, Palaeoecology* **231**, 110–119 (2006).

65. Bijl, P. K. *et al.* Paleoceanography and ice sheet variability offshore Wilkes Land, Antarctica – Part 2: Insights from Oligocene–Miocene dinoflagellate cyst assemblages. *Climate of the Past* **14**, 1015–1033 (2018).

66. Hoem, F. S. *et al.* Temperate Oligocene surface ocean conditions offshore of Cape Adare, Ross Sea, Antarctica. *Climate of the Past* **17**, 1423–1442 (2021).

67. Lavelle, M., Fielding, C. R., Hall, M. A. & Thomson, M. R. A. Molluscan stable isotope temperature estimates of the southwestern Ross Sea during the early Oligocene and early Miocene, CRP-2/2A and CRP-3, Victoria Land Basin, Antarctica. *Terra Antarctica* **8**, 439–444 (2001).

68. Leckie, R. M. & Webb, P.-N. Late Oligocene–early Miocene glacial record of the Ross Sea, Antarctica: Evidence from DSDP Site 270. *Geology* **11**, 578–582 (1983).

69. Watkins, D. K. & Villa, G. Palaeogene calcareous nannofossils from CRP-2/2A, Victoria Land Basin, Antarctica. *Terra Antartica* vol. 7 443–452 https://epic.awi.de/id/eprint/27374/ (2000).

70. Taviani, M. & Beu, A. G. The palaeoclimatic significance of Cenozoic marine macrofossil assemblages from Cape Roberts Project drillholes, McMurdo Sound, Victoria Land Basin, East Antarctica. *Palaeogeography, Palaeoclimatology, Palaeoecology* **1–2**, 131–143 (2003).

71. Ehrmann, W. Smectite content and crystallinity in sediments from CRP-2/2A, Victoria Land Basin, Antarctica. *Terra Antarctica* **7**, 575–580 (2000).

72. Powell, R. D., Krissek, L. A. & van Der Meer, J. J. M. Preliminary depositional environmental analysis of CRP-2/2A, Victoria Land Basin, Antarctica: Palaeoglaciological and palaeoclimatic inferences. *Terra Antarctica* **7**, 313–322 (2000).

73. Barrett, P. J. Cenozoic Climate and Sea Level History from Glacimarine Strata off the Victoria Land Coast, Cape Roberts Project, Antarctica. in *Glacial Sedimentary Processes and Products* (eds. Hambrey, M. J., Christoffersen, P., Glasser, N. F. & Hubbard, B.) 259–287 (Blackwell Publishing Ltd., 2007).

74. Prebble, J. G., Raine, J. I., Barrett, P. J. & Hannah, M. J. Vegetation and climate from two Oligocene glacioeustatic sedimentary cycles (31 and 24 Ma) cored by the Cape Roberts Project, Victoria Land Basin, Antarctica. *Palaeogeography, Palaeoclimatology, Palaeoecology* **231**, 41–57 (2006).

75. Passchier, S. *et al.* Early Eocene to middle Miocene cooling and aridification of East Antarctica. *Geochemistry, Geophysics, Geosystems* **14**, 1399–1410 (2013).

76. Naish, T. R. *et al.* Orbitally induced oscillations in the East Antarctic ice sheet at the Oligocene/Miocene boundary. *Nature* **413**, 719–723 (2001).

77. Roberts, A. P., Wilson, G. S., Harwood, D. M. & Verosub, K. L. Glaciation across the Oligocene-Miocene boundary in southern McMurdo Sound, Antarctica: New chronology from the CIROS-1 drill hole. *Palaeogeography, Palaeoclimatology, Palaeoecology* **198**, 113–130 (2003).

78. DeConto, R., Pollard, D. & Harwood, D. Sea ice feedback and Cenozoic evolution of Antarctic climate and ice sheets. *Paleoceanography* **22**, PA3214 (2007).

79. Houben, A. J. P. *et al.* Reorganization of Southern Ocean plankton ecosystem at the onset of Antarctic glaciation. *Science* **340**, 341–344 (2013).

80. Galeotti, S. *et al.* Antarctic Ice Sheet variability across the Eocene-Oligocene boundary climate transition. *Science* **352**, 76–80 (2016).

81. Liu, Z. *et al.* Global Cooling During the Eocene-Oligocene Climate Transition. *Science* **323**, 1187–1190 (2009).

82. Bijl, P. K. & Brinkhuis, H. A new genus and two new species of dinoflagellate cysts from lower Eocene marine sediments of the Wilkes Land Margin, Antarctica. *Review of Palaeobotany and Palynology* **220**, 88–97 (2015).

83. Pascher, K. M. *et al.* Expansion and diversification of high-latitude radiolarian assemblages in the late Eocene linked to a cooling event in the southwest Pacific. *Clim. Past* **11**, 1599–1620 (2015).

84. Scher, H. D., Bohaty, S. M., Smith, B. W. & Munn, G. H. Isotopic interrogation of a suspected late Eocene glaciation. *Paleoceanography* **29**, 2014PA002648 (2014).

85. Carter, A., Riley, T. R., Hillenbrand, C.-D. & Rittner, M. Widespread Antarctic glaciation during the Late Eocene. *Earth and Planetary Science Letters* **458**, 49–57 (2017).

86. Macphail, M. K. & Truswell, E. M. Palynology of Neogene slope and rise deposits from ODP sites 1165 and 1167, East Antarctica. *Proceedings of the Ocean Drilling Program: Scientific Results* **188**, (2004).

87. Passchier, S., Ciarletta, D. J., Miriagos, T. E., Bijl, P. K. & Bohaty, S. M. An Antarctic stratigraphic record of stepwise ice growth through the Eocene-Oligocene transition. *GSA Bulletin* **129**, 318–330 (2017).

88. Raine, J. & Askin, R. Terrestrial palynology of Cape Roberts Project Drillhole CRP-3, Victoria Land Basin, Antarctica. *Terra Antartica* **8**, 389–400 (2001).

89. Askin, R. A. Spores and pollen from the McMurdo Sound erratics, Antarctica. *Antarctic Research Series* **76**, 161–181 (2000).

90. Stilwell, J. D. & Zinsmeister, W. J. Paleobiogeographic synthesis of the Eocene macrofauna from McMurdo Sound, Antarctica. *Paleobiology and Paleoenvironments of Eocene Rocks: McMurdo Sound, East Antarctica* **76**, 365–372 (2000).

91. Willis, P. M. A. & Stilwell, J. D. A Probable Piscivorous Crocodile from Eocene Deposits of Mcmurdo Sound, East Antarctica. in *Paleobiology and Paleoenvironments of Eocene Rocks: McMurdo Sound, East Antarctica* 355–358 (American Geophysical Union (AGU), 2000). doi:10.1029/AR076p0355.

92. Pross, J. *et al.* Persistent near-tropical warmth on the Antarctic continent during the early Eocene epoch. *Nature* **487**, 73–77 (2012).